Stellar versus Galactic: the intensity of cosmic rays at the evolving Earth and young exoplanets around Sun-like stars

D. Rodgers-Lee [1],[*] A. M. Taylor,[2] A. A. Vidotto [1] and T. P. Downes[3]

[1]*School of Physics, Trinity College Dublin, University of Dublin, College Green, Dublin 2 D02 PN40, Ireland*
[2]*DESY, D-15738 Zeuthen, Germany*
[3]*Centre for Astrophysics & Relativity, School of Mathematical Sciences, Dublin City University, Glasnevin D09 W6Y4, Ireland*

ABSTRACT

Energetic particles, such as stellar cosmic rays, produced at a heightened rate by active stars (like the young Sun) may have been important for the origin of life on Earth and other exoplanets. Here, we compare, as a function of stellar rotation rate (Ω), contributions from two distinct populations of energetic particles: stellar cosmic rays accelerated by impulsive flare events and Galactic cosmic rays. We use a 1.5D stellar wind model combined with a spatially 1D cosmic ray transport model. We formulate the evolution of the stellar cosmic ray spectrum as a function of stellar rotation. The maximum stellar cosmic ray energy increases with increasing rotation, i.e. towards more active/younger stars. We find that stellar cosmic rays dominate over Galactic cosmic rays in the habitable zone at the pion threshold energy for all stellar ages considered ($t_* = 0.6$–2.9 Gyr). However, even at the youngest age, $t_* = 0.6$ Gyr, we estimate that $\gtrsim 80$ MeV stellar cosmic ray fluxes may still be transient in time. At ~ 1 Gyr when life is thought to have emerged on Earth, we demonstrate that stellar cosmic rays dominate over Galactic cosmic rays up to ~ 4 GeV energies during flare events. Our results for $t_* = 0.6$ Gyr ($\Omega = 4\ \Omega_\odot$) indicate that $\lesssim$ GeV stellar cosmic rays are advected from the star to 1 au and are impacted by adiabatic losses in this region. The properties of the inner solar wind, currently being investigated by the Parker Solar Probe and Solar Orbiter, are thus important for accurate calculations of stellar cosmic rays around young Sun-like stars.

Key words: diffusion – methods: numerical – Sun: evolution – stars: magnetic field – cosmic rays.

1 INTRODUCTION

There is much interest in determining the conditions, such as the sources of ionization for exoplanetary atmospheres, that were present in the early Solar system when life is thought to have begun on Earth (at a stellar age of ~ 1 Gyr; Mojzsis et al. 1996). This allows us to postulate what the important factors that led to life here on Earth were. These studies can then be extended to young exoplanets around solar-type stars whose atmospheres may be characterized in the near future by upcoming missions, such as the *James Webb Space Telescope* (*JWST*; Gardner et al. 2006; Barstow & Irwin 2016).

Cosmic rays represent a source of ionization (Rimmer & Helling 2013) and heating (Roble, Ridley & Dickinson 1987; Glassgold, Galli & Padovani 2012) for exoplanetary atmospheres. In this paper, we compare the contributions from two distinct populations of energetic particles: stellar cosmic rays accelerated by their host stars and Galactic cosmic rays. Galactic cosmic rays reach Earth after travelling through the heliosphere (see review by Potgieter 2013). These cosmic rays originate from our own Galaxy and constitute a reservoir of relativistic particles in the interstellar medium (ISM) that diffuse through the magnetized solar wind in a momentum-dependent way.

The propagation of Galactic cosmic rays through the stellar winds of younger solar-type stars has previously been studied (Svensmark

2006; Cohen, Drake & Kóta 2012; Rodgers-Lee et al. 2020a). The intensity of Galactic cosmic rays that reached the young Earth (~ 1 Gyr old) is thought to be much reduced in comparison to present-day observed values. This is due to the increased velocity and magnetic field strength present in the stellar wind of a young ($\sim$ Gyr old) solar-type star in comparison to the present-day solar wind (assuming that the turbulence properties of the wind remain constant with stellar age). Similar to what has been estimated to occur for Galactic cosmic rays, the changing physical conditions of the stellar wind throughout the life of a Sun-like star will affect the propagation of stellar cosmic rays. The propagation of Galactic cosmic rays through the astrospheres[1] of a number of M dwarf stars has also recently been considered (Herbst et al. 2020; Mesquita, Rodgers-Lee & Vidotto 2021).

Here, we investigate the intensity of solar, or more generally stellar, cosmic rays as they propagate through the wind of a solar-type star throughout the star's life, particularly focusing on the intensity at the orbital distance of Earth. Solar/stellar cosmic rays are also known as solar/stellar energetic particles. We focus on solar-type stars so that our results can also be interpreted in the context of the young Sun and the origin of life on Earth.

Cosmic rays are thought to be important for prebiotic chemistry and therefore may play a role in the origin of life (Dartnell 2011;

---

[*] E-mail: drodgers@tcd.ie

[1]The more general term for the heliosphere of other stellar systems.

Rimmer, Helling & Bilger 2014; Airapetian et al. 2016; Dong et al. 2019). Cosmic rays may also result in observable chemical effects in exoplanetary atmospheres by leading to the production of molecules such as NH_4^+, H_3^+, and H_3O^+ (Helling & Rimmer 2019; Barth et al. 2021). In addition to this, cosmic rays may lead to the production of *fake* biosignatures via chemical reactions involving NO_x (Grenfell et al. 2013). Biosignatures are chemical signatures that are believed to be the chemical signatures of life, such as molecular oxygen (Meadows et al. 2018). Thus, in order to interpret upcoming observations that will focus on detecting biosignatures, we must constrain the contribution of cosmic rays to fake biosignatures.

An interesting aspect that we focus on in this paper is the fact that the intensity and momentum of stellar cosmic rays accelerated by a solar-type star most likely increase for younger stars due to their stronger stellar magnetic fields, unlike the Galactic cosmic ray spectrum that is assumed to remain constant with time. The present-day Sun, despite being an inactive star, has been inferred to accelerate particles to GeV energies in strong solar flares (Ackermann et al. 2014; Ajello et al. 2014; Kafexhiu et al. 2018). There is also evidence from cosmogenic nuclides to suggest that large solar energetic particle (SEP) events occurred even in the last few thousand years (Miyake 2019). Thus, it is very likely that a younger Sun would accelerate particles at a higher rate, and to higher energies, due to the stronger magnetic field strengths observed for young Sun-like stars (e.g. Johns-Krull 2007; Hussain et al. 2009; Donati et al. 2014) and at a more continuous rate due to an increased frequency of stellar flares (Maehara et al. 2012, 2015). A scaled-up version of a large SEP event is often assumed as representative of stellar cosmic rays around main-sequence M dwarf stars or young pre-main-sequence solar-type stars. The work presented in this paper builds upon this research and aims to contribute towards a clearer and broader understanding of the spectral shape and intensity of stellar cosmic rays that reach exoplanets around solar-type stars as a function of age.

There has also been a significant amount of research concerning the propagation of stellar cosmic rays through the magnetospheres and atmospheres of close-in exoplanets around M dwarf stars (Segura et al. 2010; Tabataba-Vakili et al. 2016), as well as comparisons with Galactic cosmic rays (Grießmeier et al. 2015). Atri (2020) also investigated the surface radiation dose for exoplanets resulting from stellar cosmic ray events starting at the top of an exoplanetary atmosphere considering an atmosphere with the same composition as Earth's. Our results can be used in the future as an input for these types of studies.

In this paper, we compare the relative intensities of stellar and Galactic cosmic rays of different energies as a function of stellar age. This allows us to estimate the age of a solar-mass star when the intensities of stellar and Galactic cosmic rays are comparable, at a given energy. This also depends on the orbital distance being considered. Here, we focus mainly on the habitable zone of a solar-mass star where the presence of liquid water may be conducive to the development of life (Kasting, Whitmire & Reynolds 1993).

Previous studies have estimated the intensity of Galactic cosmic rays at ~1 Gyr when life is thought to have begun on Earth. Stellar cosmic rays have separately been considered in the context of T-Tauri systems (Rab et al. 2017; Rodgers-Lee et al. 2017, 2020b; Fraschetti et al. 2018; Offner, Gaches & Holdship 2019) and more generally in star-forming regions (see Padovani et al. 2020, for a recent review). Fraschetti et al. (2019) also investigated the impact of stellar cosmic rays for the Trappist-1 system. Scheucher et al. (2020) focused on the chemical effect of a large stellar energetic particle event on the habitability of Proxima Cen b. However, the propagation of stellar cosmic rays through stellar systems has not yet been investigated as a

function of stellar rotation rate or at the potentially critical time when the Sun was ~1 Gyr old. We also compare the relative intensities of stellar and Galactic cosmic rays for the HR2562 system (Konopacky et al. 2016) that we focused on previously in Rodgers-Lee et al. (2020a).

The paper is structured as follows: in Section 2, we describe the details of our model and the properties that we have adopted for the stellar cosmic rays. In Section 3, we present and discuss our results in relation to the young Sun and the young exoplanet, HR 2562b. Finally, we present our conclusions in Section 4.

2 FORMULATION

In this section, we motivate our stellar cosmic ray spectrum as a function of stellar rotation rate. We also briefly describe the cosmic ray transport model and stellar wind model that we use (previously presented in Rodgers-Lee et al. 2020a).

2.1 From solar to stellar cosmic rays

The present-day Sun is the only star for which we can directly detect solar cosmic rays and determine the energy spectrum of energetic particles arriving to Earth. We use these observations of the present-day Sun to guide our estimate for the stellar cosmic ray spectrum of solar-type stars of different ages, which are representative of the Sun in the past. The shape of the energy spectrum and the overall power in stellar cosmic rays are the two quantities required to describe a stellar energetic particle spectrum (Section 2.4).

SEP events can broadly be divided into two categories known as gradual and impulsive events (Reames 2013; Klein & Dalla 2017, for instance). Gradual SEP events are thought to be mainly driven by the acceleration of particles at the shock fronts of coronal mass ejections (CMEs) as they propagate. These events produce the largest fluences of protons at Earth. Impulsive SEP events are associated with flares close to the corona of the Sun and while they result in lower proton fluences at Earth they occur more frequently than gradual events. The terms 'gradual' and 'impulsive' refer to the associated X-ray signatures.

While gradual SEP events associated with CMEs produce the largest fluences of protons detected at Earth, it is unclear what energies the CMEs would have and how frequently they occur for younger solar-type stars (Aarnio, Matt & Stassun 2012; Drake et al. 2013; Osten & Wolk 2015). Very large intensities of stellar cosmic rays associated with very energetic, but infrequent, CMEs may simply wipe out any existing life (Cullings et al. 2006; Atri 2020) on young exoplanets rather than helping to kick start it. On the other hand, lower intensities of stellar cosmic rays, associated with impulsive flare events, at a more constant rate may be more of a catalyst for life (Atri 2016; Lingam et al. 2018; Dong et al. 2019). In the context of the potential impact of stellar energetic particles on exoplanetary atmospheres, we restrict our focus here to protons. This is because only protons can be accelerated to ~GeV energies, rather than electrons that suffer from energy losses.

Many white light (referring to broad-band continuum enhancement, rather than chromospheric line emission, for instance) flares have been detected by the Kepler mission (Koch et al. 2010). An increase in the frequency of superflares (bolometric flare energies of $> 10^{33}$ erg) with increasing stellar rotation (i.e. younger stars) has also been found (Maehara et al. 2015). Some of the most energetic white light flares are from pre-main-sequence stars in the Orion complex detected in the Next Generation Transit Survey (Jackman

et al. 2020). Since SEP events often have associated optical and X-ray emission, the detection of very energetic white light flares from younger stars/faster rotators is presumed to lead to a corresponding increase in X-rays. Indeed, young stars are known to be stronger X-ray sources in comparison to the Sun (Feigelson, Garmire & Pravdo 2002). Therefore, it seems likely that stars younger than the Sun will also produce more stellar energetic particles than the present-day Sun (see Herbst et al. 2021, for a recent estimate of stellar proton fluxes derived using the empirical relation between stellar effective temperature and starspot temperature).

Somewhat surprisingly, given the number of superflares detected with Kepler, there have been a small number of stellar CME candidate events (Argiroffi et al. 2019; Moschou et al. 2019; Vida et al. 2019; Leitzinger et al. 2020). To investigate the possibility that stellar CMEs are not as frequent as would be expected by extrapolating the solar flare–CME relation (Aarnio et al. 2012; Drake et al. 2013; Osten & Wolk 2015), Alvarado-Gómez et al. (2018) illustrated using magnetohydrodynamic simulations that a strong large-scale stellar dipolar magnetic field (associated with fast rotators) may suppress CMEs below a certain energy threshold. Another line of argument discussed in Drake et al. (2013) suggests that the solar flare-CME relationship may not hold for more active stars because the high CME rate expected for active stars (obtained by extrapolating the solar flare–CME relationship) would lead to very high stellar mass-loss rates. This has not been found for mass-loss rates inferred from astrospheric Ly α observations (Wood et al. 2002, 2014; Wood 2004) or from transmission spectroscopy, coupled to planetary atmospheric evaporation and stellar wind models (Vidotto & Bourrier 2017). At the same time, the number of stars with estimates for their mass-loss rates remains small.

Thus, as a first estimate for the intensity of stellar energetic particles impinging on exoplanetary atmospheres we consider flare-accelerated protons that we inject close to the surface of the star. We do not consider stellar energetic particles accelerated by shocks associated with propagating CMEs due to the current lack of observational constraints for the occurrence rate and energy of stellar CMEs as a function of stellar age. Our treatment of the impulsive stellar cosmic ray events is described in the following section.

Our investigation treats the injection of stellar cosmic rays as continuous in time during a given epoch of a star's life. Two key factors here that control the applicability of such an assumption are that young solar-type stars (i.e. fast rotators) are known to flare more frequently than the present-day Sun, and their associated flare intensity at a given frequency is more powerful (Salter, Hogerheijde & Blake 2008; Maehara et al. 2012, 2015). In order to focus on stellar cosmic rays injected at such a heightened rate and power, and thus can be treated as continuous in time, we restrict our results to stellar rotation rates greater than the rotation rate of the present-day Sun. We discuss this assumption in more detail in Section 3.3.

2.2 Transport equation for stellar cosmic rays

To model the propagation of stellar cosmic rays from a solar-type star out through the stellar system, we solve the 1D cosmic ray transport equation (derived by Parker 1965, for the modulation of Galactic cosmic rays in the Solar system), assuming spherical symmetry. We use the same numerical code as presented in Rodgers-Lee et al. (2020a) that includes spatial diffusion, spatial advection, and energy losses due to momentum advection of the cosmic rays. The 1D transport equation is given by

$$\frac{\partial f}{\partial t} = \nabla \cdot (\kappa \nabla f) - v \cdot \nabla f + \frac{1}{3} (\nabla \cdot v) \frac{\partial f}{\partial \ln p} + Q, \tag{1}$$

where $f(r, p, t)$ is the cosmic ray phase space density, $\kappa(r, p, \Omega)$ is the spatial diffusion coefficient, $v(r, \Omega)$ is the radial velocity of the stellar wind, and p is the momentum of the cosmic rays (taken to be protons).[2] Q is defined as

$$Q(r_{\text{inj}}, p, \Omega) = \frac{1}{4\pi p^2} \frac{\mathrm{d}\dot{N}}{\mathrm{d}^3 x \, \mathrm{d}p}, \tag{2}$$

which represents the volumetric injection of stellar cosmic rays per unit time and per unit interval in momentum, injected at a radius of $r_{\text{inj}} \sim 1.3 \, \mathrm{R}_{\odot}$. $\dot{N} = \mathrm{d}N/\mathrm{d}t$ is the number of particles injected per unit time. Q varies as a function of stellar rotation rate, Ω. The details of how we treat the injection rate are discussed in Section 2.4. The numerical scheme and the simulation set-up are otherwise the same as that of Rodgers-Lee et al. (2020a).

We assume an isotropic diffusion coefficient, which varies spatially by scaling with the magnetic field strength of the stellar wind (and on the level of turbulence present in it) and depends on the cosmic ray momentum (see equation 3 of Rodgers-Lee et al. 2020a). Here, for simplicity we take the level of turbulence to be independent of stellar rotation rate using the same value as motivated in Rodgers-Lee et al. (2020a). Spatial advection and the adiabatic losses of the cosmic rays depend on the velocity and divergence of the stellar wind.

In the context of the modulation of *Galactic* cosmic rays spatial and momentum advection collectively result in the suppression of the local interstellar spectrum (LIS) of Galactic cosmic rays that we observe at Earth. For *stellar* cosmic rays, the situation is slightly different due to their place of origin in the system. Stellar cosmic rays still suffer adiabatic losses as they travel through the stellar wind via the momentum advection term, but the spatial advective term now merely advects the stellar cosmic rays out through the Solar system. Spatial advection only operates as a loss term if the stellar cosmic rays are advected the whole way through and out of the stellar system.

2.3 Stellar wind model

In our model, the stellar wind of a Sun-like star is launched due to thermal pressure gradients and magneto-centrifugal forces in the hot corona overcoming stellar gravity (Weber & Davis 1967). The wind is heated as it expands following a polytropic equation of state. Stellar rotation is accounted for in our model leading to (a) angular momentum loss via the magnetic field frozen into the wind and (b) the development of an azimuthal component of an initially radial magnetic field. We use the same stellar wind model as in Rodgers-Lee et al. (2020a) that is presented in more detail in Carolan et al. (2019). Our 1.5D polytropic magneto-rotator stellar wind model (Weber & Davis 1967) is modelled with the Versatile Advection Code (VAC; Tóth 1996; Johnstone et al. 2015) and here we provide a brief summary of it.

By providing the stellar rotation rate, magnetic field, density, and temperature at the base of the wind as input parameters for the model we are able to determine the magnetic field strength, velocity and density of the stellar wind as a function of orbital distance out to 1 au. Beyond 1 au, the properties of the stellar wind are extrapolated out to the edge of the astrosphere as discussed in section 2.3.2 of Rodgers-Lee et al. (2020a). The main inputs for the stellar wind model that we varied in Rodgers-Lee et al. (2020a) to retrieve the wind properties of a solar-type star for different ages were (a) the stellar rotation rate itself (derived from observations of solar-type stars of different

---

[2]There was a typographical error in equation (1) of Rodgers-Lee et al. (2020a), where the $v \cdot \nabla f$ term was expressed as $\nabla \cdot (vf)$.

Table 1. List of parameters for the simulations. The columns are, respectively, the age (t_*) of the solar-type star, its rotation rate (Ω) in terms of the present-day solar value ($\Omega_\odot = 2.67 \times 10^{-6}\,\mathrm{rad\,s^{-1}}$), its rotation period ($P_{\mathrm{rot}}$), the astrospheric radius (R_{h}), the radial velocity ($v_{1\,\mathrm{au}}$), and the magnitude of the total magnetic field ($|B_{1\,\mathrm{au}}|$) at $r = 1$ au. $\dot{M}$ is the mass-loss rate. L_{CR} is the power we inject in stellar cosmic rays, which we relate to the kinetic power in the stellar wind. The second and third last columns are the momentum and kinetic energy for the stellar cosmic rays at which the exponential break in the injected spectrum occurs. In order to reproduce our injected cosmic ray spectrum (Q in equations 1 and 2), first, the values of L_{CR} and p_{max} given below can be used in equation (4) to determine $(\mathrm{d}\dot{N}/\mathrm{d}p)|_{2mc}$ for a given value of Ω. Then, $\mathrm{d}\dot{N}/\mathrm{d}p$, and therefore Q, can be calculated for a given value of Ω. The last column gives the kinetic energy below which the stellar cosmic ray intensities dominate over the Galactic cosmic ray intensities at 1 au.

t_* (Gyr)	Ω ($\Omega_\odot$)	P_{rot} (d)	R_{h} (au)	$v_{1\,\mathrm{au}}$ (km s^{-1})	$|B_{1\,\mathrm{au}}|$ (G)	$\dot{M}$ (M$_\odot$ yr^{-1})	$L_{\mathrm{CR}} = 0.1 P_{\mathrm{SW}}$ (erg s^{-1})	p_{max} (GeV/c)	T_{max} (GeV)	$T(j_{1\,\mathrm{au}}^{\mathrm{SCR}} = j_{1\,\mathrm{au}}^{\mathrm{GCR}})$ (GeV)
2.9	1.3	22	500	610	5.4×10^{-5}	2.8×10^{-13}	3.30×10^{27}	0.26	0.04	1.3
1.7	1.6	17	696	660	7.6×10^{-5}	5.1×10^{-13}	6.89×10^{27}	0.38	0.07	2.6
1.0	2.1	13	950	720	1.2×10^{-4}	8.5×10^{-13}	1.38×10^{28}	0.54	0.14	4.1
0.6	3.0	9	1324	790	1.8×10^{-4}	1.5×10^{-12}	2.99×10^{28}	0.85	0.33	8.0
0.6	3.5	8	1530	820	2.8×10^{-4}	2.0×10^{-12}	4.16×10^{28}	1.03	0.46	10
0.6	4.0	7	1725	850	3.5×10^{-4}	2.4×10^{-12}	5.49×10^{28}	1.23	0.61	13
0.6	3.5	8	1530	820	2.8×10^{-4}	2.0×10^{-12}	4.16×10^{28}	3.30	2.49	33

ages; Gallet & Bouvier 2013), (b) the stellar magnetic field strength (using the scaling law presented in Vidotto et al. 2014a), (c) the base temperature (using the empirical relationship with stellar rotation rate from Ó Fionnagáin & Vidotto 2018), and (d) the base density of the stellar wind (following Ivanova & Taam 2003). In the stellar wind model the base, or launching point, of the wind is chosen to be $1\,\mathrm{R}_\odot$ for the instances in time that we investigate. Table 1 provides the stellar rotation rates/ages that we consider here. The corresponding stellar surface magnetic field strength, base density, and temperature that we use are given in table 1 of Rodgers-Lee et al. (2020a). Generally, the magnetic field strengths and velocities of the stellar wind increase with increasing stellar rotation rate.

2.4 Stellar cosmic ray spectrum

We assume a continuous injection spectrum for the stellar cosmic rays such that $\mathrm{d}\dot{N}/\mathrm{d}p \propto \mathrm{d}N/\mathrm{d}p \propto p^{-\alpha}$. We adopt a power-law index of $\alpha = 2$ that in the limit of a strong non-relativistic shock is representative of diffusive shock acceleration (DSA; as first analytically derived by Krymskii 1977; Bell 1978; Blandford & Ostriker 1978) or compatible with acceleration due to magnetic reconnection. We relate the total injected kinetic power in stellar cosmic rays, L_{CR} (which we define in Section 2.4.2), to $\mathrm{d}\dot{N}/\mathrm{d}p$ in the following way

$$L_{\mathrm{CR}} = \int_0^\infty \frac{\mathrm{d}\dot{N}}{\mathrm{d}p} T(p)\,\mathrm{d}p \tag{3}$$

$$\approx \left.\frac{\mathrm{d}\dot{N}}{\mathrm{d}p}\right|_{2mc} \int_{p_0}^{p_M} \left(\frac{p}{2mc}\right)^{-\alpha} \mathrm{e}^{(-p/p_{\mathrm{max}})} T(p)\,\mathrm{d}p, \tag{4}$$

where m is the proton mass, c is the speed of light, and $T(p) = mc^2(\sqrt{1 + (p/mc)^2} - 1)$ is the kinetic energy of the cosmic rays. p_{max} is the maximum momentum that the cosmic rays are accelerated to which is discussed further in Section 2.4.1. The logarithmically spaced momentum bins for the cosmic rays are given by $p_k = \exp\{k \times \ln(p_M/p_0)/(M-1) + \ln p_0\}$ for $k = 0, ..., M$ with $M = 60$. The extent of the momentum grid that we consider ranges from $p_0 = 0.15\,\mathrm{GeV}/c$ to $p_M = 100\,\mathrm{GeV}/c$, respectively.

We have normalized the power law in equation (4) to a momentum of $2mc$ since this demarks the part of integrand which dominates the integral (for spectra in the range $2 < \alpha < 3$ of primary interest to

us). To illustrate this, following Drury, Markiewicz & Voelk (1989), equation (3) can be approximated as

$$\int_0^\infty \frac{\mathrm{d}\dot{N}}{\mathrm{d}p} T(p)\,\mathrm{d}p \approx \left.\frac{\mathrm{d}\dot{N}}{\mathrm{d}p}\right|_{2mc} \int_{p_0}^{2mc} \left(\frac{p}{2mc}\right)^{-\alpha} \mathrm{e}^{(-p/p_{\mathrm{max}})} \frac{p^2}{2m}\,\mathrm{d}p$$

$$+ \left.\frac{\mathrm{d}\dot{N}}{\mathrm{d}p}\right|_{2mc} \int_{2mc}^{p_M} \left(\frac{p}{2mc}\right)^{-\alpha} \mathrm{e}^{(-p/p_{\mathrm{max}})} pc\,\mathrm{d}p, \tag{5}$$

which has split the integral into a non-relativistic and relativistic component given by the first and second term on the right-hand side of equation (5), respectively. Equation (5) implicitly assumes that $p_0 \ll 2mc$. For $\alpha = 2$, equation (5) can be estimated as

$$L_{\mathrm{CR}} \approx p^2 \left.\frac{\mathrm{d}\dot{N}}{\mathrm{d}p}\right|_{2mc} \left[1 - \frac{p_0}{2mc} + \ln\left(\frac{p_{\mathrm{max}}}{2mc}\right)\right]. \tag{6}$$

Thus, considering $p_{\mathrm{max}} \sim 3\,\mathrm{GeV}/c$ indicates that the first and last term contribute approximately equally in equation (6). $p^2 \frac{\mathrm{d}\dot{N}}{\mathrm{d}p}|_{2mc}$ is chosen to normalize the integral to the required value of L_{CR}.

2.4.1 Spectral break as a function of stellar rotation rate

The maximum momentum of the accelerated cosmic rays, p_{max}, is another important parameter that we must estimate as a function of Ω. It physically represents the maximum momentum of stellar cosmic rays that we assume the star is able to efficiently accelerate particles to. Both DSA and magnetic reconnection rely on converting magnetic energy to kinetic energy. The magnetic field strength of Sun-like stars is generally accepted to increase with increasing stellar rotation rate, or decreasing stellar age (Vidotto et al. 2014a; Folsom et al. 2018). This indicates that more magnetic energy would have been available at earlier times in the Sun's life or for other stars rotating faster/younger than the present-day Sun to produce stellar cosmic rays.

Therefore, we evolve p_{max} as a function of stellar magnetic field strength. In our model, this effectively means that the maximum injected momentum evolves as a function of stellar rotation rate. We assume that

$$p_{\mathrm{max}}(\Omega) = p_{\mathrm{max},\odot}\left(\frac{B_*(\Omega)}{B_{*,\odot}}\right). \tag{7}$$
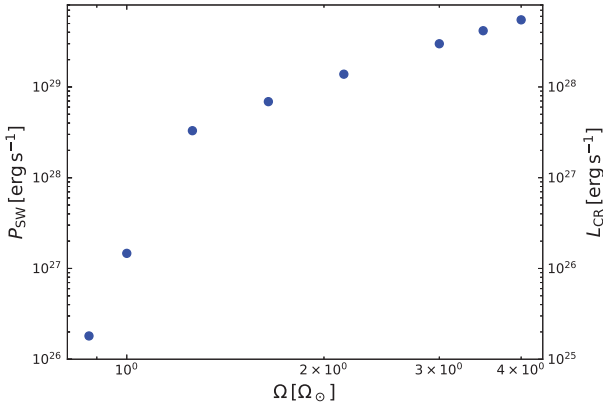
Figure 1. Kinetic power in the solar wind, P_{SW}, as a function of stellar rotation rate. The right-hand side of the plot indicates the total kinetic power that we inject in stellar cosmic rays corresponding to 10 per cent of P_{SW}.
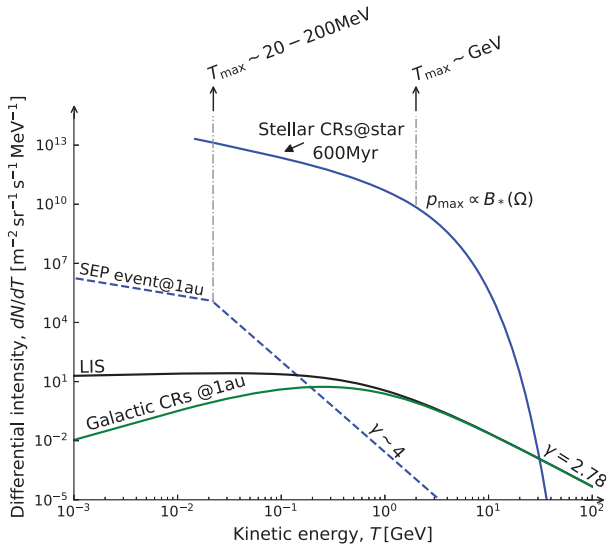

Figure 2. This sketch illustrates typical cosmic ray spectra, both solar/stellar (impulsive and gradual events) and Galactic in origin, at various orbital distances in the solar/stellar system. The solid black line represents an approximation for the LIS of Galactic cosmic rays outside of the Solar system. The green line represents a typical Galactic cosmic ray spectrum observed at Earth. The blue dashed line is a typical spectrum for a gradual SEP event (averaged over the duration of the event). The spectral slope γ at high energies is also indicated in the plot. The solid blue line is the estimate for an impulsive stellar energetic particle event spectrum that we motivate in this paper for a young solar-type star ($\sim$600 Myr old) which includes a spectral break at much higher energies than the typical present-day (gradual) SEP spectrum (blue dashed line). See Section 2.5 for more details.

We chose $p_{max,\odot} = 0.2$ GeV/c, corresponding to a kinetic energy of $T_{max} = 20$ MeV (Kouloumvakos et al. 2015, for instance, report impulsive stellar energetic particle events with kinetic energies $\gtrsim$ 50 MeV). We also investigate the effect of assuming $p_{max,\odot} = 0.6$ GeV/c (corresponding to $T_{max} = 200$ MeV). The values for $p_{max}(\Omega)$ are given in Table 1. The maximum value that we use is 3.3 GeV/c for a stellar rotation rate of 3.5 $\Omega_\odot$ at $t_* = 600$ Myr using $p_{max,\odot} = 0.6$ GeV/c. In comparison, Padovani et al. (2015) estimated a maximum energy of $\sim$30 GeV for the acceleration of protons at protostellar surface shocks for $t_* \lesssim 1$ Myr. The maximum momentum of 3.3 GeV/c that we adopt corresponds to a surface average large-scale magnetic field of $\sim$8 G at 600 Myr. If we

investigated younger stellar ages when it would be reasonable to adopt an average large-scale stellar magnetic field of $\sim$80 G then we would also find a maximum energy of $\sim$30 GeV.

Equation (7) is motivated by the Hillas criterion (Hillas 1984) which estimates that the maximum momentum achieved at a shock can be obtained using

$$p_{max}c \sim q\beta_s B_s R_s = \frac{1}{c}\left(\frac{v}{100\,\text{km s}^{-1}}\right)\left(\frac{B}{10\,\text{G}}\right)\left(\frac{R}{10^9\,\text{cm}}\right)\text{GeV},$$
$$(8)$$

where $\beta_s = v_s/c$ and v_s is the characteristic velocity associated with the scattering agent giving rise to acceleration (e.g. shock velocity or turbulence velocity), B_s is the magnetic field strength within the source, and R_s is the size of the source region. If we assume that the size of the emitting region (a certain fraction of the Sun's surface) and the characteristic velocity do not change as a function of stellar rotation rate, we simply obtain $p_{max} \propto B_s$ as adopted in equation (7).

Indeed, high-energy γ-ray observations from *Fermi*-LAT found that for strong solar flares the inferred proton spectrum, located close to the surface of the Sun, displays a high maximum kinetic energy break of $\gtrsim$ 5 GeV (Ackermann et al. 2014; Ajello et al. 2014). Generally, the spectral break occurs at lower kinetic energies, or momenta, for less energetic but more frequent solar flares. Since the power law break in the SEP spectrum shifts to higher energies during strong solar flares, this is a good indicator that p_{max} is likely to have occurred at higher momenta in the Sun's past when solar flares were more powerful. For instance, Atri (2017) uses a large SEP event as a representative spectrum for an M dwarf star that has a higher cut-off energy at approximately $\sim$GeV energies.

2.4.2 Total kinetic power in stellar cosmic rays

We use the kinetic power in the stellar wind, $P_{SW} = \dot{M}(\Omega)v_\infty(\Omega)^2/2$, calculated from our stellar wind model to estimate L_{CR} as a function of stellar rotation rate assuming a certain efficiency, shown in Fig. 1. $\dot{M}(\Omega)$ and $v_\infty(\Omega)$ are the mass-loss rate and terminal speed of the stellar wind, respectively. Here, we assume that $L_{CR} \sim 0.1P_{SW}$ that is shown on the right-hand side of Fig. 1. Such a value is typical of the equivalent efficiency factor estimated for supernova remnants (Vink et al. 2010, for instance). Without further evidence to go by, we simply adopt the same value here for young stellar flares. Adopting a different efficiency of 1 per cent or 100 per cent, for instance, would change the values for the differential intensity of stellar cosmic rays presented in Section 3 by a factor of 0.1 and 10, respectively. The values that we use here are broadly in line with the value of $L_{CR} \sim 10^{28}$ erg s^{-1} from Rodgers-Lee et al. (2017) that was motivated as the kinetic power of stellar cosmic rays produced by a T-Tauri star.

2.5 Comparison of solar, stellar, and Galactic cosmic ray spectra

We include a schematic in Fig. 2 that shows representative values for the differential intensity of solar and Galactic cosmic rays as a function of kinetic energy. The differential intensity of cosmic rays, j, is often considered (rather than the phase space density given in equation 1) as a function of kinetic energy which we plot in Section 3. These quantities are related by $j(T) = dN/dT = p^2 f(p)$.

Fig. 2 includes the estimate for our most extreme steady-state spectrum for stellar cosmic rays injected close to the stellar surface for $\Omega = 4\,\Omega_\odot$ or $t_* = 600$ Myr (solid blue line). This is representative of an impulsive stellar energetic particle event. The spectral break occurs at $\sim$GeV energies as motivated in the previous section. The

resulting spectrum at 1 au (and other orbital distances) is presented in Section 3.

A fit to the Galactic cosmic ray LIS, constrained by the *Voyager 1* observations (Stone et al. 2013; Cummings et al. 2016; Stone et al. 2019) outside of the heliosphere, is denoted by the solid black line in Fig. 2 (equation 1 from Vos & Potgieter 2015). A fit to the modulated Galactic cosmic ray spectrum measured at Earth is given by the solid green line (using the modified force field approximation given in equation 10 of Rodgers-Lee et al. 2020a, with $\phi = 0.09$ GeV). We also indicate the spectral slope, $\gamma = 2.78$, at high energies on the plot. Note, this represents $dN/dT \propto T^{-\gamma}$ rather than $dN/dp \propto p^{-\alpha}$. The power law indices γ and α are related. At relativistic energies, $\gamma = \alpha$ since $T = pc$ and at non-relativistic energies $\alpha = 2\gamma - 1$. It is important to note that the measurements at Earth change a certain amount as a function of the solar cycle. Here, however, we treat the LIS and the Galactic cosmic ray spectrum at Earth as constant when making comparisons with the stellar cosmic ray spectrum as a function of stellar rotation rate.[3]

On the other hand, the differential intensities for SEPs observed at Earth cannot be treated as constant in time. The SEP spectrum at 1 au, shown by the blue dashed line in Fig. 2, is not continuous in time for the present-day Sun. The differential intensity given by the dashed blue line represents the typical intensities of SEPs at Earth that are derived from time-averaged observations of particle fluences (such as those presented in Mewaldt et al. 2005). This spectrum is representative of a gradual SEP event. This type of SEP event lasts approximately a few days.

Rab et al. (2017) estimated the stellar cosmic ray spectrum for a young pre-main-sequence star (shown in their fig. 2) representing the present-day values for a typical gradual SEP event multiplied by a factor of 10^5 (the motivation for which is given in Feigelson et al. 2002). Tabataba-Vakili et al. (2016) similarly use a typical spectrum for a gradual SEP event and scale it with $1/R^2$ to 0.153 au in order to find the values for the differential intensity of stellar cosmic rays at the location of a close-in exoplanet orbiting an M dwarf star. In both of these examples, the spectral shape is held constant, whereas here it is not. The propagation of stellar cosmic rays from the star/CME through the stellar system is not the focus of either of these papers. This type of treatment for estimating the spectrum of stellar cosmic ray events at 1 au, or other orbital distances, around younger stars (and later type stars) and the impact of the underlying assumptions are what we investigate in this paper. This can be used as a starting point towards deriving more realistic stellar cosmic ray spectra in the

future that can be constrained by upcoming missions like *JWST* and Ariel (Tinetti et al. 2018).

Transmission spectroscopy using *JWST* will be able to detect emission features from molecules in exoplanetary atmospheres. Stellar and Galactic cosmic rays should produce the same chemical reactions. Thus, close-in exoplanets around young and/or active stars are the best candidates to detect the chemical signatures of stellar cosmic rays as they should be exposed to high stellar cosmic ray fluxes. In comparison, the Galactic cosmic ray fluxes at these orbital distances should be negligible. Helling & Rimmer (2019) and Barth et al. (2021) identify a number of 'fingerprint ions' whose emission, if detected in an exoplanetary atmosphere, would be indicative of ionization by cosmic rays. These fingerprint ions are ammonium (NH_4^+) and oxonium (H_3O^+). Barth et al. (2021) also suggest that stellar and Galactic cosmic rays contribute (along with other forms of high-energy radiation, such as X-rays) to the abundance of the following key organic molecules: hydrogen cyanide (HCN), formaldehyde (CH_2O), and ethylene (C_2H_4). Barth et al. (2021) indicate that CH_2O and C_2H_4 may be abundant enough to possibly be detected by *JWST*.

2.6 Overview of the simulations

We consider seven cosmic ray transport simulations in total for our results. Additional test case simulations are presented in Appendix A for physical set-ups with known analytical solutions verifying that our numerical method reproduces well these expected results. Six of the seven simulations that we ran represent the result of varying the stellar rotation rate. The remaining simulation, for $\Omega = 3.5\,\Omega_\odot$, investigates the effect of increasing the value of the p_{max} which is discussed in Appendix 2.4.1. The parameters for the simulations are shown in Table 1.

The values for the astrospheric radii, $R_h(\Omega)$, are given in Table 1 which is the outer radial boundary. These values were derived by balancing the stellar wind ram pressure against the ram pressure of the ISM (see section 2.3.3 of Rodgers-Lee et al. 2020a). The logarithmically spaced radial bins for $i = 0, ..., N$ are given by $r_i = \exp\{i \times \ln(r_N/r_0)/(N-1) + \ln r_0\}$ where $r_0 = 1\,R_\odot$ and $r_N = R_h(\Omega)$ with $N = 60$.

3 RESULTS

In this section, we investigate the evolution of the stellar cosmic ray spectrum at different orbital distances as a function of stellar rotation rate. Five parameters vary with Ω for these simulations: $B(r)$, $v(r)$, R_h, L_{CR}, and p_{max}. The value of R_h does not play much of a role in our simulations since it is always much larger than the orbital distances that we are interested in.

After travelling through the stellar wind, stellar cosmic rays can interact with a planet's atmosphere. If a planetary magnetic field is present this will also influence the propagation of the stellar cosmic rays through the atmosphere (e.g. Grießmeier et al. 2015). Higher energy cosmic rays will be less easily deflected by an exoplanetary magnetic field. Cosmic rays with energies that are capable of reaching the surface of an exoplanet are of interest for the origin of life. For this, the pion production threshold energy of 290 MeV should be significant. Pions produce secondary particles that can trigger particle showers (as discussed in Atri 2020, for instance). Sufficiently energetic secondary particles, such as neutrons, can reach the surface of a planet which are known as ground level enhancements. Solar neutrons have been detected even on Earth with neutron monitors since the 1950s (Simpson 1951). Thus, our aim is to determine the
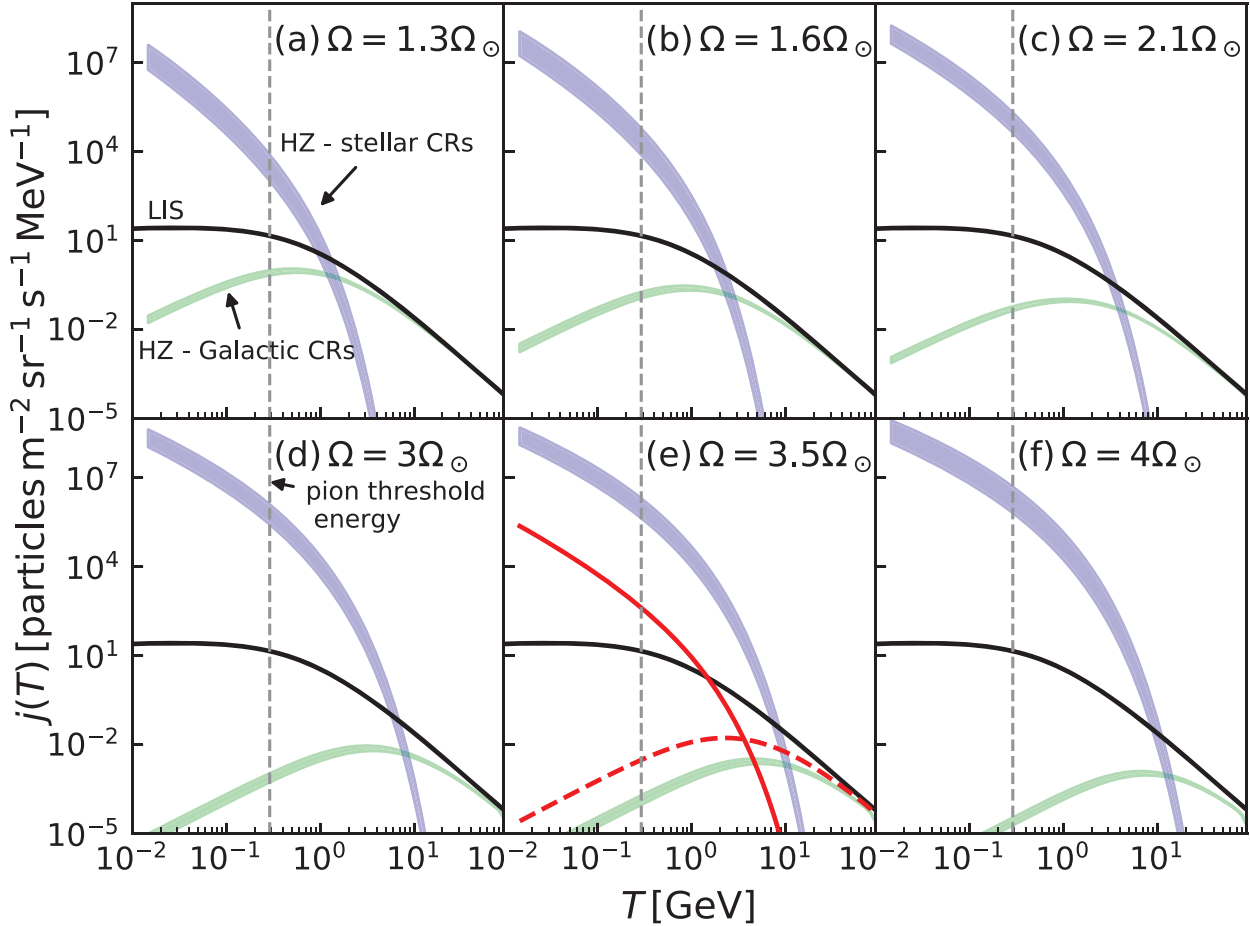
---

[3]It is important to note that the Galactic cosmic ray LIS may have been different in the past. Supernova remnants are believed to be a major contributor to the Galactic component of the LIS (Drury 1983, 2012). The star formation rate (SFR, which can be linked to the number of supernova remnants using an initial mass function) of the Milky Way in the past therefore should influence the LIS in the past. For instance, high ionization rates (with large uncertainties) have been inferred for galaxies at high redshifts that have higher SFRs than the present-day Milky Way (Muller et al. 2016; Indriolo et al. 2018). In these studies, the inferred ionization rate is attributed to Galactic cosmic rays. Recently, using observations of the white dwarf population in the solar neighbourhood ($d < 100$ pc), Isern (2019) reconstructed an effective SFR for the Milky Way in the past. They found evidence of a peak in star formation $\sim$2.2–2.8 Gyr ago, an increase by a factor of $\sim$3 in comparison to the present-day SFR. Using a sample of late-type stars, Rocha-Pinto et al. (2000) also found an increase in the SFR by a factor of $\sim$2.5 approximately 2–2.5 Gyr ago. Since these results suggest that the SFR has been within a factor of $\sim$3 of its present-day value for the stellar ages that we focus on, we did not vary the LIS fluxes with stellar age in Rodgers-Lee et al. (2020a).

Figure 3. The differential intensity of stellar cosmic rays (blue shaded regions) and Galactic cosmic rays (green shaded regions) in the habitable zone as a function of kinetic energy. Each panel represents a different value for the stellar rotation rate. $\Omega = 2.1\,\Omega_\odot$ corresponds to $t_* = 1$ Gyr, shown in (c), when life is thought to have begun on Earth. Also shown are the differential intensities of stellar (solid red line) and Galactic cosmic rays (red dashed line) at 20 au, the orbital distance of HR 2562b, in panel (e). The black solid line is a fit to the *Voyager 1* data for the LIS. The grey dashed line represents the pion threshold energy, 290 MeV. See text in Section 3.1.

range of stellar rotation rates for which the differential intensity of stellar cosmic rays dominates over Galactic cosmic rays at energies above the pion threshold energy.

3.1 Stellar cosmic rays as a function of stellar rotation rate (or age)

Fig. 3 shows the stellar cosmic ray differential intensities as a function of kinetic energy for our simulations. In each of the panels, the blue shaded region represents the values of differential intensities for stellar cosmic rays present in the habitable zone for a solar-mass star. For comparison, the green shaded region shows the differential intensities for Galactic cosmic rays in the habitable zone (from the simulations presented in Rodgers-Lee et al. 2020a).

The habitable zone of a solar-mass star evolves with stellar age that we have incorporated in the shaded regions of Fig. 3. We follow the formalism of Selsis et al. (2007) with the recent Venus and early Mars criteria, using the stellar evolutionary model of Baraffe et al. (1998). At 600 Myr, the young Sun was less luminous and had an effective temperature slightly smaller than its present-day value. Thus, the habitable zone at 600 Myr was located closer to the Sun between $r \sim$ 0.64–1.58 au in comparison to the present-day values of $r \sim 0.72$–

1.77 au (using the recent Venus and early Mars criteria). Given the finite resolution of our spatial grid some of the blue shaded regions in Fig. 3 are slightly smaller than the calculated habitable zone. Finally, for comparison in each of the panels the solid black line shows the LIS values (from Vos & Potgieter 2015). The vertical grey dashed line represents the pion threshold energy at 290 MeV.

Figs 3(a)–(f) show at the pion threshold energy that stellar cosmic rays dominate over Galactic cosmic rays in the habitable zone for all values of stellar rotation rate (or age) that we consider. The energy that they dominate up to differs though as a function of stellar rotation rate (given in Table 1). For instance, at $\Omega = 1.3\,\Omega_\odot$, the transition from stellar cosmic rays dominating over Galactic cosmic rays occurs at ~ 1.3 GeV. It increases up to ~ 13 GeV for $\Omega = 4\,\Omega_\odot$. The stellar cosmic ray fluxes also increase in the habitable zone as a function of stellar rotation rate. At the same time, the Galactic cosmic ray fluxes decrease.

The red dashed line and solid lines in Fig. 3(e) are the values for the differential intensities at 20 au for Galactic and stellar cosmic rays, respectively. We previously discussed the Galactic cosmic ray differential intensities for $\Omega = 3.5\,\Omega_\odot$ (Fig. 3e here) in Rodgers-Lee et al. (2020a) in the context of the HR2562 exoplanetary system. HR2562 is a young solar-like star with a warm Jupiter exoplanet orbiting at
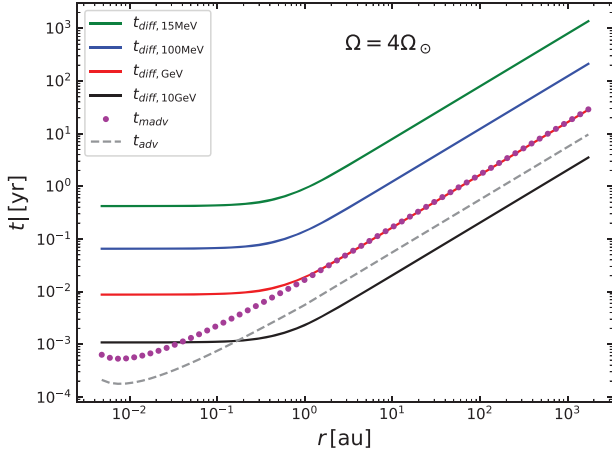
Figure 4. Time-scales for the different physical processes for the stellar wind properties corresponding to a stellar rotation rate of $\Omega = 4\,\Omega_\odot$, corresponding to $t_* \sim 600$ Myr. The solid lines represent the diffusion time-scale for cosmic rays with different energies. The magenta dotted line and the grey dashed line represent the momentum advection and advection time-scales, respectively. For 10 GeV cosmic rays, $t_{madv} \lesssim t_{diff}$ at $r \lesssim 0.03$ au and $t_{madv} \lesssim t_{diff}$ at $r \lesssim 0.5$ au for GeV energies. This illustrates the importance of adiabatic losses for the stellar cosmic rays at small orbital distances.
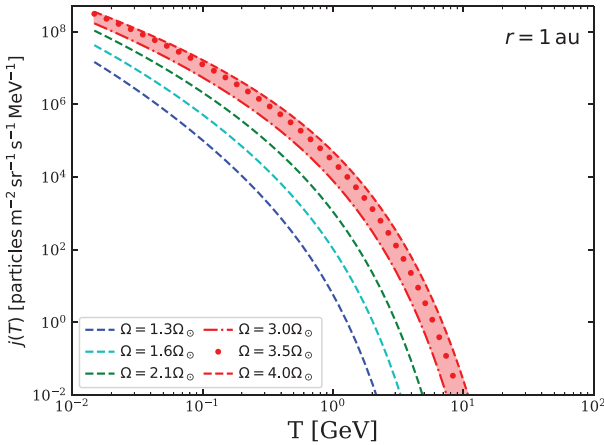
Figure 5. Plot of the differential intensities for different stellar rotation rates at 1 au. The shaded red region represents different stellar rotation rates corresponding to the same stellar age, namely 600 Myr.

20 au. Although Galactic cosmic rays (dashed red line) represent a source of continuous cosmic ray flux, stellar cosmic rays can dominate (solid red line) at approximately the orbital distance of the exoplanet for $\lesssim 5$ GeV. This would happen at times of impulsive events.

The solid blue line in Fig. 2 shows the steady-state spectrum close to the star corresponding to $\Omega = 4\,\Omega_\odot$. By comparing with the values for the fluxes found in the habitable zone, shown in Fig. 3(f), we can determine by how many orders of magnitude the stellar cosmic ray fluxes have decreased between $\sim 1\,R_\odot$ and ~ 1 au ($\sim 200\,R_\odot$). The decrease is slightly greater than 4 orders of magnitude. The decrease is the combined result of diffusive and advective processes. In Appendix A, we discuss the effect of the different physical processes, shown in Fig. A1.

Fig. 4 shows the time-scales for the different physical processes for $\Omega = 4\,\Omega_\odot$. The diffusion time-scales for 0.015, 0.1, 1, and 10 GeV energy cosmic rays are shown by the solid lines in Fig. 4 where $t_{diff} = r^2/\kappa(r, p, \Omega)$. The magenta dots represent an estimate

for the momentum advection time-scale $t_{madv} \sim 3r/v$. For $r \lesssim 1$ au, Fig. 4 shows that the spatial and momentum advection time-scales are shorter than the diffusion time-scale for cosmic rays with kinetic energies $\lesssim$ GeV. These low-energy cosmic rays are affected by adiabatic losses in this region and are being advected by the stellar wind, rather than propagating diffusively. Since the stellar cosmic rays are injected close to the surface of the star only the cosmic rays with kinetic energies $\gtrsim$ GeV, and therefore short diffusion time-scales, propagate diffusively out of this region.

We also investigated the sensitivity of our results on our choice of p_{max} in Appendix 2.4.1. Fig. B1 shows the results of adopting a higher maximum cosmic ray momentum for $\Omega = 3.5\,\Omega_\odot$. We find that the location of the stellar cosmic ray spectral break is an important parameter to constrain and that it affects our results significantly, with the maximum energy at which stellar cosmic rays dominate Galactic cosmic rays being an increasing function of p_{max}.

3.2 Differential intensities as a function of rotation rate at 1 au

Fig. 5 shows the differential intensities of the stellar cosmic rays at 1 au as a function of Ω. The differential intensities obtained at 1 au increase as a function of stellar rotation rate. The increase in the differential intensities is almost entirely due to the corresponding increase in L_{CR}. The red shaded region indicates the values for different stellar rotation rates with the same stellar age, $t_* = 600$ Myr. The shift in the maximum energy to higher energies with increasing stellar rotation rate can also be seen by comparing the $\Omega = 1.3\,\Omega_\odot$ (dashed blue line) and $\Omega = 4\,\Omega_\odot$ (dashed red line) cases. The slope of the spectrum at 10^{-2}–1 GeV energies becomes less steep with increasing stellar rotation and starts to turn over at slightly higher energies.

3.3 Assumption of continuous injection

Fig. 3 shows that the intensities of stellar cosmic rays are greater than those of the Galactic cosmic rays at energies around the pion energy threshold for all values of stellar rotation rate that we consider. However, we must also estimate the energy up to which these stellar cosmic rays can be treated as continuous in time.

In order for the stellar cosmic ray flux to be considered continuous, the rate of flare events (producing the stellar cosmic rays) must be larger than the transport rate for a given cosmic ray energy. We use $1/t_{diff}$ at $\lesssim 1$ au where it is approximately independent of radius as a reference value for the transport rate. We estimate the maximum stellar cosmic ray energy which can be taken as continuous by considering the relation between flare energy and flare frequency ($dN/dE_{flare} \propto E_{flare}^{-1.8}$ from Maehara et al. 2015). First, from fig. 4 of Maehara et al. (2015) we can obtain the flare rate, by multiplying the flare frequency by the flare energy, as a function of flare energy. Fig. 2 of Maehara et al. (2015) also indicates that stars with rotation periods between 5–10 d flare approximately 10 times more frequently than slow rotators, like the Sun. Thus, as an estimate we increase the flare rate by an order of magnitude for fast rotators as a function of flare energy (fig. 4 of Maehara et al. 2015). We determine p_{max} for a given flare energy by equating the flare energy with magnetic energy such that $E_{flare} \propto B^2$ (similar to Herbst et al. 2021). Therefore, using the Hillas criterion given in equation (8), $p_{max} \propto E_{flare}^{1/2}$.

In Fig. 6, we plot the flare rate (solid lines) and diffusion rates (dashed lines) as a function of momentum. The diffusive time-scale for the slow rotator/$\sim$solar case is based on the stellar wind properties presented in Rodgers-Lee et al. (2020a) for the present-day Sun, $\Omega = 1\,\Omega_\odot$. For the slow rotator/solar case, this plot indicates

that the maximum continuously injected cosmic ray momentum is $p_{c,\,max} = 0.11\,\mathrm{GeV}/c$ ($T_{c,\,max} = 5$ MeV). For fast rotators, it indicates that $p_{c,max} = 0.4\,\mathrm{GeV}/c$ ($T_{max} = 80$ MeV). Thus, even for our most extreme case, flare-injected stellar cosmic rays cannot be considered as continuous beyond 80 MeV in energy. The plot has been normalized such that $\sim$GeV cosmic ray energies correspond to $E_{flare} \sim 10^{33}$ erg. It is important to note that here we have determined quite low values of $p_{c,max}$ by comparing the diffusive transport rate with the flare rate. However, a comparison of the flare rate with the chemical recombination rates in exoplanetary atmospheres may result in higher values for $p_{c,max}$.

4 DISCUSSION AND CONCLUSIONS

In this paper, we have investigated the differential intensity of stellar cosmic rays that reach the habitable zone of a solar-type star as a function of stellar rotation rate (or age). We motivated a new spectral shape for stellar cosmic rays that evolves as a function of stellar rotation rate. In particular, the maximum injected stellar cosmic ray energy and total injected stellar cosmic ray power evolve as a function of stellar rotation rate. We consider stellar cosmic rays injected at the surface of the star, which would be associated with stellar flares whose solar counterparts are known as impulsive SEP events. The values for the total injected stellar cosmic ray power and the maximum stellar cosmic ray energy that we provide in this paper can be used to reproduce our injected stellar cosmic ray spectrum. We then used the results of a 1.5D stellar wind model for the stellar wind properties (from Rodgers-Lee et al. 2020a) in combination with a 1D cosmic ray transport model to calculate the differential intensity of stellar cosmic rays at different orbital distances.

Our main findings are that, close to the pion threshold energy, stellar cosmic rays dominate over Galactic cosmic rays at Earth's orbit for the stellar ages that we considered, $t_* = 0.6$–$2.9\,\mathrm{Gyr}$ ($\Omega = 1.3$–$4\,\Omega_\odot$). Stellar cosmic rays dominate over Galactic cosmic rays up to ~ 10 GeV energies for stellar rotation rates >3 $\Omega_\odot$, corresponding approximately to a stellar age of 600 Myr. The differential intensities of the stellar cosmic rays increase with stellar rotation rate, almost entirely due to the increasing stellar cosmic ray luminosity. At 1 Gyr, when life is thought to have begun on Earth, we find that high fluxes of stellar cosmic rays dominate over Galactic cosmic rays up to 4 GeV energies. However, based on stellar flare rates, we estimate that the stellar cosmic ray fluxes may only be continuous in time up to MeV energies even for the fastest rotator cases that we consider. For momenta where the diffusive transport rate is larger than the flare rate, the flare injection cannot be treated as continuous. The transition point corresponds to $p_{c,max} = 0.1$ and $0.4\,\mathrm{GeV}/c$, or to $T_{c,max} = 5$ and $80\,\mathrm{MeV}$, for the slow rotator/solar and young solar cases, respectively.

Our results overall highlight the importance of considering stellar cosmic rays in the future for characterizing the atmospheres of young close-in exoplanets. They also highlight the possible importance of stellar cosmic rays for the beginning of life on the young Earth and potentially on other exoplanets.

We find for the young exoplanet HR 2562b, orbiting its host star at 20 au, that stellar cosmic rays dominate over Galactic cosmic rays up to ~ 4 GeV energies despite the large orbital distance of the exoplanet. However, these stellar cosmic ray fluxes may not be continuous in time.

Our results presented in Fig. 3, for a stellar age of 600 Myr ($\Omega = 4$ $\Omega_\odot$), demonstrate that low-energy stellar cosmic rays ($<$GeV) move advectively as they travel out through the stellar wind from the injection region to 1 au. In this region, the low-energy cosmic rays are also
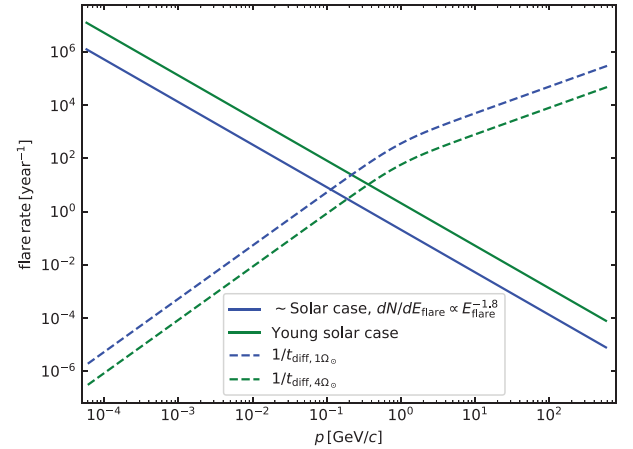

Figure 6. Plot of flare rate (flare frequency from Maehara et al. 2015, times E_{flare}) as a function of $p_{c,max}$ for a slow rotator like the Sun (with $P_{rot} > 20$ d, solid blue line) and for fast rotators (with $P_{rot} = 5$–10 d, solid green line) at 1 au. The diffusive transport rate as a function of momentum is overplotted for $\Omega = 1\,\Omega_\odot$ and $\Omega = 4\,\Omega_\odot$ by the dashed blue and green lines, respectively.

impacted by adiabatic losses. Beyond 1 au, the low-energy cosmic rays are influenced to a greater extent by diffusion. This finding is quite interesting because the velocity of the solar wind at close distances is currently unknown. NASA's Parker Solar Probe (Bale et al. 2019) and ESA's Solar Orbiter (Owen et al. 2020) have only recently begun to probe the solar wind at these distances. Thus, our simulation results are sensitive to parameters of the solar wind that are only now being observationally constrained. If the solar wind is faster in this region than what we have used in our models, then the fluxes of stellar cosmic rays that we calculate at larger radii will be smaller.

Our results are based on a 1D cosmic ray transport model coupled with a 1.5D stellar wind model. In reality, stellar winds are not spherically symmetric. Latitudinal variations are seen in the solar wind that also depend on the solar cycle (e.g. McComas et al. 2003) and magnetic maps of other low-mass stars also show that the magnetic field structure is not azimuthally symmetric (e.g. Llama et al. 2013; Vidotto et al. 2014b). Gradients in the magnetic field can lead to particle drifts that we cannot investigate with our models. Our results are based on steady-state simulations, which means that effects occurring on time-scales shorter than the rotation period of the star are neglected in the cosmic ray transport model. The fact that flares may also occur at positions on the stellar surface that then do not reach Earth is not taken into account in our models. It will be of great interest in the future to use 2D or 3D cosmic ray transport models in combination with 3D stellar wind models (e.g. Kavanagh et al. 2019; Folsom et al. 2020) to study in greater detail the stellar cosmic ray fluxes reaching known exoplanets. Our results represent some type of average behaviour that could be expected: at particular times during a stellar cycle, the stellar cosmic ray production rate via flares could be increased, whereas at other times during the minimum of a stellar cycle the production rate would be lower. However, due to the present lack of observational constraints for the stellar cosmic ray fluxes in other stellar systems, using a simple 1D cosmic ray transport model and a 1.5D stellar wind model is justified.

Finally, it is also worth bearing in mind that the stellar cosmic rays considered here are representative of impulsive events. The stellar cosmic ray fluxes produced by CMEs are likely to be far in excess of those presented here. These fluxes would be even more transient in nature than the stellar cosmic ray fluxes presented here. In light of

these findings, future modelling of stellar cosmic rays from transient flare events and gradual events appears motivated.

DATA AVAILABILITY

The output data underlying this article are available at https://doi.org/10.5281/zenodo.4707597.

REFERENCES

Aarnio A. N., Matt S. P., Stassun K. G., 2012, ApJ, 760, 9
Ackermann M.et al., 2014, ApJ, 787, 15
Airapetian V. S., Glocer A., Gronoff G., Hébrard E., Danchi W., 2016, Nat. Geosci., 9, 452
Ajello M. et al., 2014, ApJ, 789, 20
Alvarado-Gómez J. D., Drake J. J., Cohen O., Moschou S. P., Garraffo C., 2018, ApJ, 862, 93
Argiroffi C., Reale F., Drake J. J., Ciaravella A., Testa P., Bonito R., Miceli M., Orlando S., Peres G., 2019, Nat. Astron., 3, 742
Atri D., 2016, J. R. Soc. Interface, 13, 20160459
Atri D., 2017, MNRAS, 465, L34
Atri D., 2020, MNRAS, 492, L28
Bale S. D. et al., 2019, Nature, 576, 237
Baraffe I., Chabrier G., Allard F., Hauschildt P. H., 1998, A&A, 337, 403
Barstow J. K., Irwin P. G. J., 2016, MNRAS, 461, L92
Barth P., Helling C., Stüeken E. E., Bourrier V., Mayne N., Rimmer P. B., Jardine M., Vidotto A. A., Wheatley P. J., Fares R., 2020, MNRAS, 502, 6201
Bell A. R., 1978, MNRAS, 182, 147
Blandford R. D., Ostriker J. P., 1978, ApJ, 221, L29
Carolan S., Vidotto A. A., Loesch C., Coogan P., 2019, MNRAS, 489, 5784
Cohen O., Drake J. J., Kóta J., 2012, ApJ, 760, 85
Cullings H. M., Fujita S., Funamoto S., Grant E. J., Kerr G. D., Preston D. L., 2006, Radiat. Res., 166, 219
Cummings A. C., Stone E. C., Heikkila B. C., Lal N., Webber W. R., Jóhannesson G., Moskalenko I. V., Orlando E., Porter T. A., 2016, ApJ, 831, 18
Dartnell L. R., 2011, Astrobiology, 11, 551
Donati J. F. et al., 2014, MNRAS, 444, 3220
Dong C. F., Lingam M., Fang X. H., Rimmer P. B., Wordsworth W., 2019, The First Billion Years: Habitability, Producing Conditions Conducive to Life, Vol. 2134, Lunar and Planetary Institute, Universities Space Research Association Houston Repository, USA, p. 1046
Drake J. J., Cohen O., Yashiro S., Gopalswamy N., 2013, ApJ, 764, 170
Drury L. O., 1983, Rep. Prog. Phys., 46, 973
Drury L. O. C., 2012, Astropart. Phys., 39, 52
Drury L. O., Markiewicz W. J., Voelk H. J., 1989, A&A, 225, 179
Feigelson E. D., Garmire G. P., Pravdo S. H., 2002, ApJ, 572, 335
Folsom C. P., Bouvier J., Petit P., Lèbre A., Amard L., Palacios A., Morin J., Donati J. F., Vidotto A. A., 2018, MNRAS, 474, 4956
Folsom C. P., Ó Fionnagáin D., Fossati L., Vidotto A. A., Moutou C., Petit P., Dragomir D., Donati J. F., 2020, A&A, 633, A48
Fraschetti F., Drake J. J., Cohen O., Garraffo C., 2018, ApJ, 853, 112
Fraschetti F., Drake J. J., Alvarado-Gómez J. D., Moschou S. P., Garraffo C., Cohen O., 2019, ApJ, 874, 21
Gallet F., Bouvier J., 2013, A&A, 556, A36
Gardner J. P. et al., 2006, Space Sci. Rev., 123, 485
Glassgold A. E., Galli D., Padovani M., 2012, ApJ, 756, 157
Grenfell J. L. et al., 2013, Astrobiology, 13, 415
Grießmeier J. M., Tabataba-Vakili F., Stadelmann A., Grenfell J. L., Atri D., 2015, A&A, 581, A44
Helling C., Rimmer P. B., 2019, Phil. Trans. R. Soc. A, 377, 20180398
Herbst K., Papaioannou A., Airapetian V. S., Atri D., 2021, ApJ, 907, 89
Herbst K., Scherer K., Ferreira S. E. S., Baalmann L. R., Engelbrecht N. E., Fichtner H., Kleimann J., Toit Strauss R. D., Moeketsi D. M., Mohamed S., 2020, ApJ, 897, L27
Hillas A. M., 1984, ARA&A, 22, 425
Hussain G. A. J. et al., 2009, MNRAS, 398, 189
Indriolo N., Bergin E. A., Falgarone E., Godard B., Zwaan M. A., Neufeld D. A., Wolfire M. G., 2018, ApJ, 865, 127
Isern J., 2019, ApJ, 878, L11
Ivanova N., Taam R. E., 2003, ApJ, 599, 516
Jackman J. A. G. et al., 2020, MNRAS , 497, 809
Johns-Krull C. M., 2007, ApJ, 664, 975
Johnstone C. P., Güdel M., Lüftinger T., Toth G., Brott I., 2015, A&A, 577, A27
Kafexhiu E., Romoli C., Taylor A. M., Aharonian F., 2018, ApJ, 864, 148
Kasting J. F., Whitmire D. P., Reynolds R. T., 1993, Icarus, 101, 108
Kavanagh R. D., 2019, MNRAS, 485, 4529
Klein K.-L., Dalla S., 2017, Space Sci. Rev., 212, 1107
Koch D. G. et al., 2010, ApJ, 713, L79
Konopacky Q. M. et al., 2016, ApJ, 829, L4
Kouloumvakos A. et al., 2015, A&A, 580, A80
Krymskii G. F., 1977, Akademiia Nauk SSSR Dokl., 234, 1306
Leitzinger M. et al., 2020, MNRAS, 493, 4570
Lingam M., Dong C., Fang X., Jakosky B. M., Loeb A., 2018, ApJ, 853, 10
Llama J., Vidotto A. A., Jardine M., Wood K., Fares R., Gombosi T. I., 2013, MNRAS, 436, 2179
McComas D. J., Elliott H. A., Schwadron N. A., Gosling J. T., Skoug R. M., Goldstein B. E., 2003, Geophys. Res. Lett., 30, 1517
Maehara H., Shibayama T., Notsu S., Notsu Y., Nagao T., Kusaba S., Honda S., Nogami D., Shibata K., 2012, Nature, 485, 478
Maehara H., Shibayama T., Notsu Y., Notsu S., Honda S., Nogami D., Shibata K., 2015, Earth, Planets, Space, 67, 59
Meadows V. S., Reinhard C. T., Arney G. N., Parenteau M. N., Schwieterman E. W., 2018, Astrobiology, 18, 630
Mesquita A. L., Rodgers-Lee D., Vidotto A. A., 2021 , MNRAS, submitted
Mewaldt R. A., Cohen C. M. S., Labrador A. W., Leske R. A., Mason G. M., Desai M. I., Looper M. D., Mazur J. E., Selesnick R. S., Haggerty D. K., 2005, J. Geophys. Res., 110, A09S18
Miyake F., 2019, 36th International Cosmic Ray Conference (ICRC2019) Vol. 36 of International Cosmic Ray Conference, Cosmogenic Evidences for Past SEP Events. p. 11, Available at: https://doi.org/10.22323/1.358.0011
Mojzsis S. J., Arrhenius G., McKeegan K. D., Harrison T. M., Nutman A. P., Friend C. R. L., 1996, Nature, 384, 55
Moschou S.-P., Drake J. J., Cohen O., Alvarado-Gómez J. D., Garraffo C., Fraschetti F., 2019, ApJ, 877, 105
Muller S. et al., 2016, A&A, 595, A128
Ó Fionnagáin D., Vidotto A. A., 2018, MNRAS, 476, 2465
Offner S. S. R., Gaches B. A. L., Holdship J. R., 2019, ApJ, 883, 121
Osten R. A., Wolk S. J., 2015, ApJ, 809, 79
Owen C. J., Bruno R., Livi S., Louarn P., Al Janabi K., Allegrini F., Amoros C., Baruah R., Barthe A., Berthomier M., Bordon S., 2020, A&A, 642, A16
Padovani M., Hennebelle P., Marcowith A., Ferrière K., 2015, A&A, 582, L13
Padovani M. et al., 2020, Space Sci. Rev., 216, 29
Parker E. N., 1965, Planet. Space Sci., 13, 9
Potgieter M. S., 2013, Living Rev. Sol. Phys., 10, 3

Rab C., Güdel M., Padovani M., Kamp I., Thi W.-F., Woitke P., Aresu G., 2017, A&A, 603, A96

Reames D. V., 2013, Space Sci. Rev., 175, 53

Rimmer P. B., Helling C., 2013, ApJ, 774, 108

Rimmer P. B., Helling C., Bilger C., 2014, Int. J. Astrobiology, 13, 173

Roble R. G., Ridley E. C., Dickinson R. E., 1987, J. Geophys. Res., 92, 8745

Rocha-Pinto H. J., Scalo J., Maciel W. J., Flynn C., 2000, A&A, 358, 869

Rodgers-Lee D., Taylor A. M., Ray T. P., Downes T. P., 2017, MNRAS, 472, 26

Rodgers-Lee D., Vidotto A. A., Taylor A. M., Rimmer P. B., Downes T. P., 2020, MNRAS, 499, 2124

Rodgers-Lee D., Taylor A. M., Downes T. P., Ray T. P., 2020, MNRAS, 491, 4742

Salter D. M., Hogerheijde M. R., Blake G. A., 2008, A&A, 492, L21

Scheucher M., Herbst K., Schmidt V., Grenfell J. L., Schreier F., Banjac S., Heber B., Rauer H., Sinnhuber M., 2020, ApJ, 893, 12

Segura A., Walkowicz L. M., Meadows V., Kasting J., Hawley S., 2010, Astrobiology, 10, 751

Selsis F., Kasting J. F., Levrard B., Paillet J., Ribas I., Delfosse X., 2007, A&A, 476, 1373

Simpson J. A., 1951, Phys. Rev., 83, 1175

Stone E. C., Cummings A. C., McDonald F. B., Heikkila B. C., Lal N., Webber W. R., 2013, Science, 341, 150

Stone E. C., Cummings A. C., Heikkila B. C., Lal N., 2019, Nat. Astron., 3, 1013

Svensmark H., 2006, Astron. Nachr., 327, 871

Tabataba-Vakili F., Grenfell J. L., Grießmeier J. M., Rauer H., 2016, A&A, 585, A96

Tinetti G. et al., 2018, Exp. Astron., 46, 135

Tóth G., 1996, Astrophys. Lett. Commun., 34, 245

Vida K., Leitzinger M., Kriskovics L., Seli B., Odert P., Kovács O. E., Korhonen H., van Driel-Gesztelyi L., 2019, A&A, 623, A49

Vidotto A. A., Bourrier V., 2017, MNRAS, 470, 4026

Vidotto A. A. et al., 2014, MNRAS, 441, 2361

Vidotto A. A., Jardine M., Morin J., Donati J. F., Opher M., Gombosi T. I., 2014, MNRAS, 438, 1162

Vink J., Yamazaki R., Helder E. A., Schure K. M., 2010, ApJ, 722, 1727

Vos E. E., Potgieter M. S., 2015, ApJ, 815, 119

Weber E. J., Davis Leverett J., 1967, ApJ, 148, 217

Wood B. E., 2004, Living Rev. Sol. Phys., 1, 2

Wood B. E., Müller H.-R., Zank G. P., Linsky J. L., 2002, ApJ, 574, 412

Wood B. E., Müller H.-R., Redfield S., Edelman E., 2014, ApJ, 781, L33

APPENDIX A: TEST CASES

We present three simulations to illustrate that the code reproduces the expected analytical results for a number of simple test cases. We isolate the effect of different physical terms in equation (1), giving additional insight into the system. The test cases use the stellar wind parameters for the $\Omega = 3.5\,\Omega_\odot$ simulation unless explicitly stated otherwise. For all of the test simulations, the same power law is injected as described in equation (4) with $p_{max} = 1.03\,\mathrm{GeV}/c$ and $L_{CR} = 4.16 \times 10^{28}\,\mathrm{erg\,s^{-1}}$.

The three test cases are simulations with: (a) a constant diffusion coefficient only, (b) the momentum-dependent diffusion coefficient derived from the magnetic field profile for $\Omega = 3.5\,\Omega_\odot$ only, and (c) the diffusion coefficient used for (b) along with the spatial and momentum advection terms. These test cases are described below in more detail. The results from these tests are shown in Fig. A1 for 1 au.

The first test case consisted of using a constant diffusion coefficient in momentum and space with $-v \cdot \nabla f = ((\nabla \cdot v)/3)(\partial f/\partial \ln p) = 0$ from equation (1) ($\kappa/\beta c = 0.07$ au using $B = 10^{-5}$ G). Thus, a continuous spatial point source injection close to the origin (at $\sim 1.3\,\mathrm{R_\odot}$ in our case) with a p^{-2} profile in momentum should result in a steady-state solution with the same momentum power law of p^{-2} at all radii until
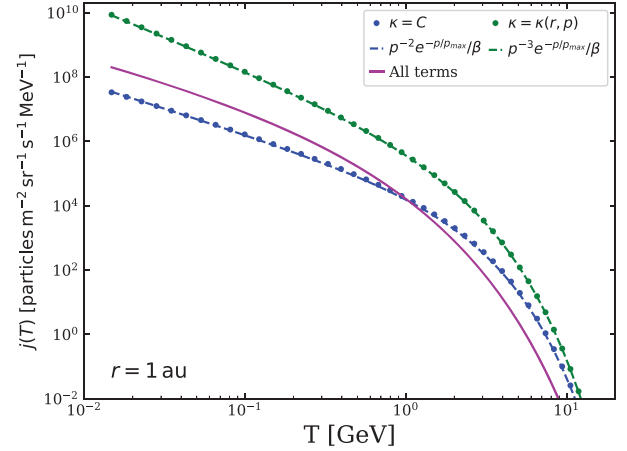

Figure A1. The differential intensity for stellar cosmic rays as a function of kinetic energy at 1 au are shown here for a number of test cases, described in Section A. The blue dots are the values obtained using a constant diffusion coefficient, test case (a). The green dots represent the model with only spatial diffusion, test case (b). Finally, the magenta solid line includes all terms considered in our models, test case (c). Different power laws are shown by the dashed lines.

the cosmic rays escape from the spatial outer boundary. The blue dots in Fig. A1 represent the cosmic ray intensities as a function of kinetic energy from the simulation at $r \sim 1$ au. The dashed line overplots a $p^{-2}\mathrm{e}^{-p/p_{max}}/\beta$ profile for comparison and show that our results match well the expected result.

The second case (green dots in Fig. A1) illustrates the effect of a spatially varying diffusion coefficient that also depends on momentum [$\kappa = \kappa(r, p)$, as is used in the simulations generally and using the magnetic field profile for the $\Omega = 3.5\,\Omega_\odot$ case]. For a continuous spatial point source injection, the particles now diffuse in a momentum-dependent way and the expected profile is $p^{-3}\mathrm{e}^{-p/p_{max}}/\beta$. The green dashed line overplots a $p^{-3}\mathrm{e}^{-p/p_{max}}/\beta$ profile for comparison and shows that our results match well the expected result.

Finally, we include all three terms in the transport equation which is shown by the solid magenta line in Fig. A1. In comparison to the diffusion only case, the cosmic ray fluxes are decreased at 1 au by nearly 2 orders of magnitude due to spatial and momentum advection.

APPENDIX B: INFLUENCE OF THE MAXIMUM MOMENTUM

Here, we investigate the sensitivity of our results on our choice of $p_{max,\odot}$ that is used to normalize the scaling relation in equation (7). We increase $p_{max,\odot}$ to 0.6 GeV/c, increasing the maximum momentum to 3.3 GeV/c for $\Omega = 3.5\,\Omega_\odot$. We compare the results of the simulation using this higher maximum momentum with the value adopted in the previous section. Fig. B1 shows the differential intensities obtained from these simulations. The red dashed line in Fig. B1 represents the results obtained using $p_{max} = 3.30$ GeV/c. The red dots are the same as the results shown in Fig. 5 using the lower value of $p_{max} = 1.03$ GeV/c. The red dash–dotted line represents the differential intensities for Galactic cosmic rays at 1 au. The effect of changing the maximum momenta is quite significant. The higher spectral break means that stellar cosmic rays would dominate over Galactic cosmic ray fluxes up to $\sim$33 GeV, in comparison to $\sim$10 GeV for the lower spectral break.
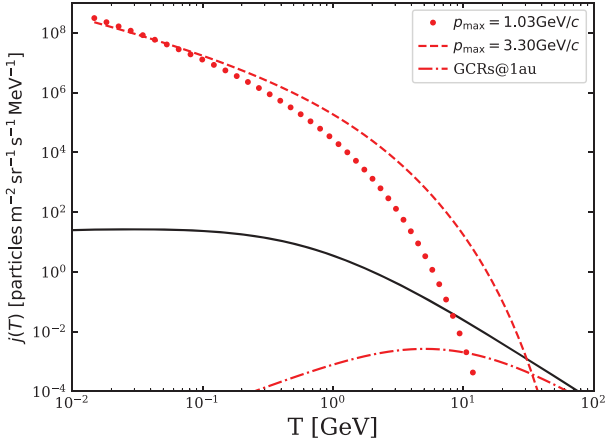
Figure B1. The differential intensities for stellar (with two different spectral breaks) and Galactic cosmic rays at 1 au are plotted for $\Omega = 3.5\,\Omega_\odot$. The dotted lines represent the same values as in Fig. 5.

This increase in the intensities occurs because of the time-scales for the different physical processes (shown in Fig. 4 for $\Omega = 4\,\Omega_\odot$). By increasing the spectral break to 3.3GeV/c, there are sufficient numbers of $\gtrsim$GeV energy cosmic rays that can avoid momentum losses in the innermost region of the stellar wind.

This paper has been typeset from a TeX/LaTeX file prepared by the author.